Intrinsic Membrane Properties Determine Hippocampal Differential Firing Pattern In Vivo in Anesthetized Rats

Janina Kowalski,[1,2]* Jian Gan,[1] Peter Jonas,[1] and Alejandro J. Pernía-Andrade[1,3,4]*

Abstract: The hippocampus plays a key role in learning and memory. Previous studies suggested that the main types of principal neurons, dentate gyrus granule cells (GCs), CA3 pyramidal neurons, and CA1 pyramidal neurons, differ in their activity pattern, with sparse firing in GCs and more frequent firing in CA3 and CA1 pyramidal neurons. It has been assumed but never shown that such different activity may be caused by differential synaptic excitation. To test this hypothesis, we performed high-resolution whole-cell patch-clamp recordings in anesthetized rats in vivo. In contrast to previous in vitro data, both CA3 and CA1 pyramidal neurons fired action potentials spontaneously, with a frequency of ~3–6 Hz, whereas GCs were silent. Furthermore, both CA3 and CA1 cells primarily fired in bursts. To determine the underlying mechanisms, we quantitatively assessed the frequency of spontaneous excitatory synaptic input, the passive membrane properties, and the active membrane characteristics. Surprisingly, GCs showed comparable synaptic excitation to CA3 and CA1 cells and the highest ratio of excitation versus hyperpolarizing inhibition. Thus, differential synaptic excitation is not responsible for differences in firing. Moreover, the three types of hippocampal neurons markedly differed in their passive properties. While GCs showed the most negative membrane potential, CA3 pyramidal neurons had the highest input resistance and the slowest membrane time constant. The three types of neurons also differed in the active membrane characteristics. GCs showed the highest action potential threshold, but displayed the largest gain of the input-output curves. In conclusion, our results reveal that differential firing of the three main types of hippocampal principal neurons in vivo is not primarily caused by differences in the characteristics of the synaptic input, but by the distinct properties of synaptic integration and input-output transformation. © 2015 The Authors Hippocampus Published by Wiley Periodicals, Inc.

KEY WORDS: hippocampal microcircuits; in vivo patch-clamp recording; passive and active membrane properties; action potentials; postsynaptic potentials

INTRODUCTION

The hippocampus plays a key role in higher brain functions, including spatial coding (O'Keefe and Dostrovsky, 1971; Hafting et al., 2005) and episodic memory (Scoville and Milner, 1957). The three types of principal neurons, the dentate granule cells (GCs), the CA3 pyramidal neurons, and the CA1 pyramidal neurons are connected to each other by glutamatergic synapses to form the classical trisynaptic circuit (Andersen et al., 1971). Several forms of information processing are believed to take place in this synaptic chain. These include pattern separation (Leutgeb et al., 2007; de Almeida et al., 2009a), pattern completion (Marr, 1971; Nakazawa et al., 2002), grid-to-place cell code conversion (Hafting et al., 2005; de Almeida et al., 2009b), and association of specific information and context by hippocampal and entorhinal inputs converging on the same cell (Lisman, 1999). How these computations are performed at the level of synapses, cells, and microcircuits is, however, largely unclear.

Although the properties of synaptic transmission and action potential (AP) initiation have been extensively studied in brain slices in vitro (Spruston and Johnston, 1992; Major et al., 1994; Lübke et al., 1998; Schmidt-Hieber et al., 2007), it is not known whether these findings can be extrapolated to in vivo conditions. In contrast to the in vitro situation, hippocampal neurons in vivo will be exposed to ongoing synaptic activity and a complex mixture of neuromodulators. Both factors are expected to change the functional properties of neurons and synapses. Conversely, while there is a huge amount of information about the firing of hippocampal neurons from extracellular recordings in vivo in anesthetized and awake behaving rodents (Harris et al., 2001; Henze et al., 2002; Buzsáki, 2004; Mizuseki et al., 2013, 2013), the intracellular synaptic events preceding AP generation cannot be probed with these experimental techniques. Clearly, high-resolution intracellular recordings are required to study the temporal characteristics of

[1] **IST Austria (Institute of Science and Technology Austria), Klosterneuburg, Austria;** [2] **Psychiatric University Clinics (UPK) Basel, Switzerland;** [3] **Department of Structural and Computational Biology, University of Vienna, Austria;** [4] **Institute of Molecular Pathology, Vienna Biocenter, Austria**

Additional Supporting Information may be found in the online version of this article.

Grant sponsor: Fonds zur Förderung der Wissenschaftlichen Forschung; Grant number: P 24909-B24; Grant sponsor: European Union (European Research Council Advanced Grant; Grant number: 268548).

*Correspondence to: Alejandro J. Pernía-Andrade, Department of Structural and Computational Biology, University of Vienna, Institute of Molecular Pathology, Dr. Bohr-Gasse 7-9, Vienna Biocenter, A-1030, Austria. E-mail: alejandro.pernia@univie.ac.at (or) Janina Kowalski, Psychiatric University Clinics (UPK) Basel, Wilhelm Klein-Strasse 27, CH-4012 Basel, Switzerland. E-mail: janina.kowalski@upkbs.ch

Accepted for publication 16 November 2015.
DOI 10.1002/hipo.22550
Published online 00 Month 2015 in Wiley Online Library (wileyonlinelibrary.com).

synaptic events in vivo, the passive and active properties of neurons in intact circuits, and the conversion of synaptic input into AP output.

To address these questions, we used whole-cell patch-clamp techniques to record from hippocampal neurons in vivo (Margrie et al., 2002; Lee et al., 2006; Pernía-Andrade and Jonas, 2014). In particular, we focused on CA3 pyramidal neurons, because they play a key role in higher network functions (Lisman, 1999; Rolls, 2013) and because their properties are largely unclear under in vivo conditions. We analyzed the spontaneous firing of the hippocampal principal neurons and determined the underlying synaptic and cellular mechanisms. Our results demonstrate that the three major types of hippocampal neurons in vivo differ in the properties of input-output transformation, indicating cell type-specific signal processing in the hippocampal network.

MATERIALS AND METHODS

Anesthesia and Preparation

Whole-cell patch-clamp recordings in vivo from neurons of the dorsal hippocampus were performed in 77 anesthetized, 27- to 31-day-old Wistar rats of either sex. The experimental procedures were modified after previous protocols (Margrie et al., 2002; Lee et al., 2006; Pernía-Andrade et al., 2012) and carried out in strict accordance with institutional, national, and European guidelines for animal experimentation. Animal experiments were approved by the Bundesministerium für Wissenschaft, Forschung und Wirtschaft of Austria (BMWF-66.018/0008-II/3b/2010).

For recording of spontaneous AP activity, light isoflurane anesthesia was used (~1.7% isoflurane vaporized in O_2 at 200–300 ml min^{-1}, Forane™, AbbVie; 15 out of 55 CA3 pyramidal neurons, 13 out of 13 CA1 pyramidal neurons, 6 out of 18 GCs). The isoflurane was delivered via a ventilation mask. For the analysis of intrinsic passive and active properties of the neurons, either light isoflurane anesthesia was used, or deep anesthesia was induced by an intraperitoneal injection of an anesthetic cocktail (MMF) comprised of 0.3 mg kg^{-1} medetomidine (Pfizer), 8 mg kg^{-1} midazolam (Roche), and 0.01 mg kg^{-1} fentanyl (Janssen-Cilag). Animals were maintained under deep anesthesia by periodic subcutaneous injection (50-min intervals) of 15–25% of the initial dose, with 100% of gaseous O_2 continuously provided via a ventilation mask.

For experiments, animals were mounted in a stereotaxic frame (David Kopf Instruments). Surgery was performed as previously described (Pernía-Andrade and Jonas, 2014). The surface of the brain was superfused with physiological saline solution containing 137 mM NaCl, 3.5 mM KCl, 1.8 mM $CaCl_2$, 1 mM $MgCl_2$, and 5 mM HEPES (pH adjusted to 7.2 with NaOH). Heart rate and arterial O_2 saturation were constantly monitored (PulseSense™ Vet, medair). Typically, the heart rate was > 260 beats per minute, and arterial O_2 saturation ranged between 97 and 100%. Body temperature was continuously monitored by a rectal thermometer and maintained at 36.5 ± 0.5°C by placing the rat on a heating plate. To test the consistency of our results under the different anesthetics, the effects of isoflurane and MMF on passive and active properties of a subpopulation of CA3 pyramidal neurons were compared; this assessment resulted in no statistical differences of passive and active properties recorded between both anesthetics.

Patch-Clamp Recording In Vivo

Patch pipettes were fabricated from borosilicate glass tubing (1.0 mm outer diameter, 0.5 mm inner diameter; Hilgenberg) with a P-1000 Brown-Flaming micropipette puller (Sutter Instrument). The pipettes had a tip resistance of 4–8 MΩ before seal formation, and were electrically connected to the patch-clamp amplifier (USB EPC10 Quadro, HEKA) through a 0.3 mm Ag/AgCl wire. A common reference electrode (Ag/AgCl pellet) was placed on the skull near the craniotomy window.

For patch-clamp recordings, the pipette solution contained (solution with high/low Cl^- concentration, respectively): 120 or 136 mM K^+-gluconate, 20 or 4 mM KCl, 10 mM EGTA, 2 mM $MgCl_2$, 2 mM Na_2ATP, 10 mM HEPES, and 0.2% biocytin (pH adjusted to 7.28 with KOH; 310 ± 5 mOsm). For the analysis of spontaneous firing and synaptic events, only solution with low Cl^- concentration was used.

Patch-clamp recordings from neurons in vivo were obtained as previously described (Pernía-Andrade and Jonas, 2014). Briefly, after seal formation (seal resistance ≥ 5 GΩ), spontaneous firing was first assessed in the cell-attached (CA) configuration at −70 mV in voltage-clamp mode (30–120 s after seal formation). Subsequently, whole-cell current-clamp (CC) experiments were performed at the resting membrane potential (V_{rest}). After the experiment, the integrity of the seal was verified by formation of an outside-out patch during withdrawal of the pipette in ~40% of cells; properties of cells with and without outside-out patch formation were not noticeably different. Pipette capacitance and series resistance (R_s) were compensated using a bridge balance circuit. Only neurons with stable R_s ($\leq$ 90 MΩ; 60 ± 2 MΩ, 86 cells; $< \pm 20\%$ change during the recording period) were used for subsequent analysis. The R_s values are consistent with those recorded at deep brain areas ($> \sim 1000$ μm; Margrie et al., 2002). All cells included in this study had average membrane potentials of ≤ -50 mV for pyramidal neurons and ≤ -65 mV for GCs, as well as overshooting APs. Membrane potential (V_m) values reported were not corrected for liquid junction potentials.

Post-Hoc Morphological Analysis

After successful recording, animals were sacrificed by decapitation. Brains were rapidly removed from the skull and immersed for at least 24 h in a 100-mM phosphate-buffered solution containing 2.5% paraformaldehyde, 1.25% glutaraldehyde, and 15% saturated picric acid. Removing the septal pole of the hemispheres permitted quick diffusion of the fixative into the region of the hippocampus. After fixation, brains were cut into 200-μm-thick parasagittal slices. The biocytin-labeled

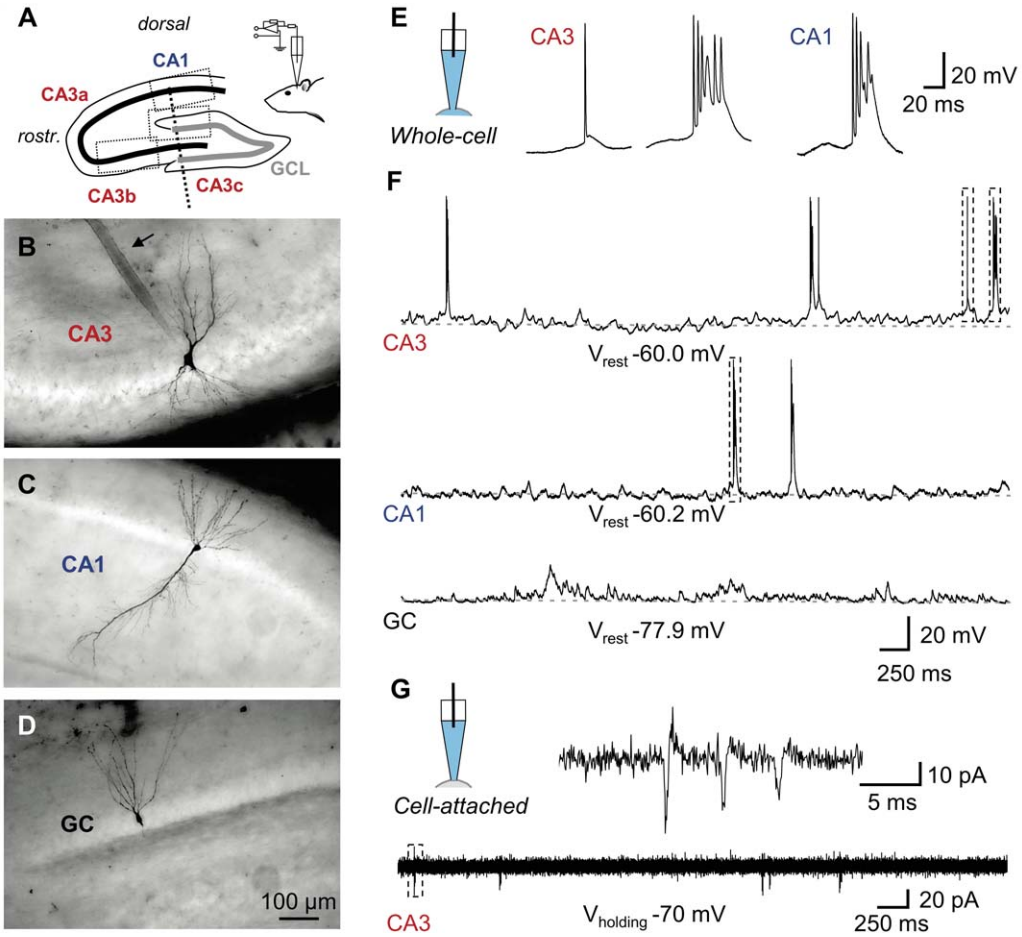

FIGURE 1. Recording from morphologically identified hippocampal principal neurons in vivo. A: Scheme of a parasagittal section through the principal cell layers of the hippocampus (thick black line, CA3a–c and CA1 pyramidal neuron layer; thick gray line, GCL; the border between CA3b and c is marked by a dashed line. Somatic positions for the neurons in B–D are indicated by dotted boxes. Patch pipettes were inserted roughly parallel to the vertical axis (inset). B–D: Extended focal images of a recorded CA3 pyramidal neuron (B), CA1 pyramidal neuron (C), and GC in the upper blade of dentate gyrus (D). All cells included in this study have been unequivocally identified by post-hoc morphological analysis. Note the prominent patch-pipette track in B (arrow). E,F: Whole-cell recordings of spontaneous firing. E: Scheme of the recording configuration (left), spontaneous single AP and AP burst (middle) in a CA3 pyramidal neuron and a burst in a CA1 pyramidal neuron (right) on expanded time scale. F: Voltage traces from a CA3 pyramidal neuron, a CA1 pyramidal neuron, and a GC on compressed time scale. Dashed boxes in the top trace indicate the APs shown in E. G: Cell-attached recording from a CA3 pyramidal neuron at expanded (top) and compressed (bottom) time scale as indicated by the scheme of the recording configuration on the top left. Note that both single APs and bursts were recorded in the cell-attached configuration, similar to the whole-cell configuration. [Color figure can be viewed in the online issue, which is available at wileyonlinelibrary.com.]

structures were visualized using avidin-biotin-peroxidase complex and 3,3'-diaminobenzidine tetrahydrochloride (DAB) as chromogen. Thereafter, the slices were embedded in an aqueous mounting medium (Mowiol, Roth).

Morphological properties of recorded cells such as dendritic and axonal arborization, somatic position, and location of the recording site, were captured both in detail and in extended focal images along the z-axis by means of a light microscope (Olympus BX61). This allowed an unequivocal identification of mature GCs, CA3 and CA1 pyramidal neurons (Figs. 1B–D; Amaral, 1978; Scharfman, 1993; Schmidt-Hieber et al., 2004). In CA3 pyramidal neurons, both dendritic and somatic recordings were obtained.

Data Acquisition and Analysis

Cell-attached and whole-cell CC recordings were performed. The signals were filtered at 10 kHz (low-pass Bessel filter), digitized at 20 kHz, and stored using Patchmaster v2x60 acquisition software running on a PC under Windows 7.

Spontaneous firing frequency

Analyses of interspike intervals (ISI) were performed to estimate the instantaneous firing frequency of the neurons. The population of bursts of APs was separated from that of single APs by calculating a critical interspike interval (ISI_{crit}; Figs. 2C,D). Briefly, a cumulative distribution function (CDF) of

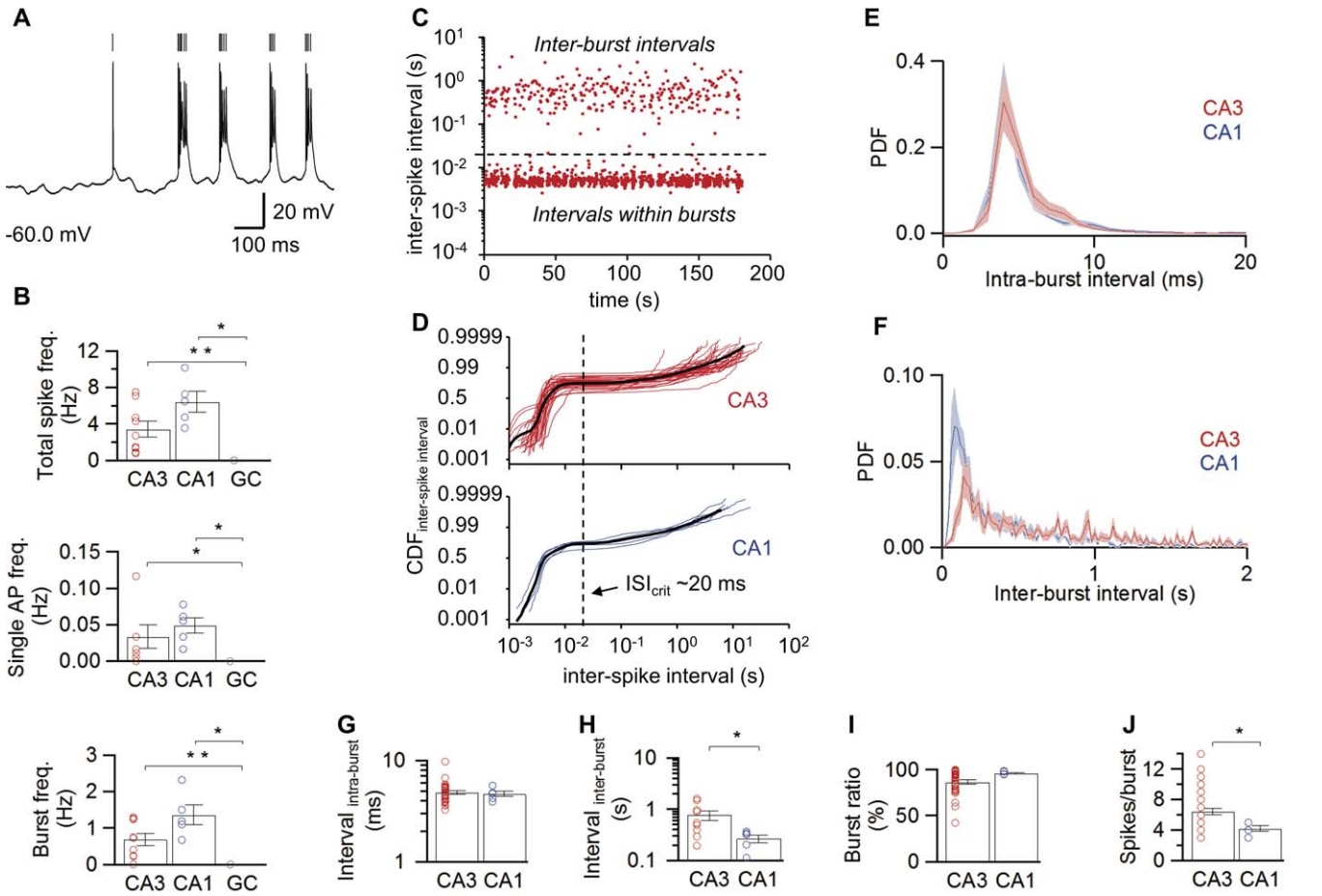

FIGURE 2. Differential spontaneous firing in hippocampal principal neurons in vivo. A: Detection of spontaneous APs in a representative CA3 pyramidal neuron; vertical lines indicate detected APs. B: Summary bar graphs of total spike, single AP, and burst frequencies. Note that all firing frequencies were markedly larger in CA3 and CA1 pyramidal neurons than in dentate gyrus GCs. C: Plot of ISI against recording time for a representative CA3 pyramidal neuron. Note the clear separation of two populations of intervals by a line at ~20 ms. D: CDF of ISI, illustrated in a double logarithmic plot for CA3 (top, 34 cells) and CA1 (bottom, 5 cells) pyramidal neurons. Thin lines represent individual experiments, thick curves show average. Vertical dashed lines represent the point of minimal slope in the CDF, corresponding to the point of separation between ISI within bursts and interburst intervals (ISI_{crit}). E,F: Probability density functions (PDF) of intraburst (E; 34 CA3 PNs, 5 CA1 PNs) and interburst intervals (F; 9 CA3 PNs, 5 CA1 PNs). Bands indicate 95% confidence intervals. G,H: Summary bar graphs of ISI within bursts (G) and between bursts (H). I,J: Summary bar graphs of burst ratio (I) and number of spikes per burst (J; 34 CA3 PNs, 5 CA1 PNs). Note that the mean interburst interval was longer, while the mean number of APs per burst was significantly larger in CA3 than in CA1 pyramidal neurons. In B and G–J, bars indicate mean ± SEM, symbols indicate data from individual experiments. *, $P < 0.05$; **, $P < 0.001$. [Color figure can be viewed in the online issue, which is available at wileyonlinelibrary.com.]

inter-spike-intervals was plotted on a double-logarithmic scale, and ISI_{crit} was defined as the point of minimal slope. Intervals $\leq ISI_{crit}$ were referred to as ISIs within bursts, whereas intervals $> ISI_{crit}$ were classified as interburst intervals. Spontaneous firing was assessed in a period of 3–4 min without current injection, providing a sufficiently large number of > 40 single APs and/or bursts per cell.

Excitatory postsynaptic potential (EPSP) and inhibitory postsynaptic potential (IPSP) detection

EPSPs were detected using a deconvolution-based algorithm (Pernía-Andrade et al., 2012) during 30 s of the spontaneous CC recording at V_{rest}. Traces were low-pass filtered at 1 kHz before analysis. Bandpass-filtered templates (10–100 Hz) with rise and decay time constants as well as EPSP amplitude were generated for each neuron and used for deconvolution-based detection. The detection threshold (θ) was set to 5 times the standard deviation (SD) of a Gaussian function fit to the baseline component of the deconvolution signal. This setting resulted in a false positive event rate of 5.8 10^{-3} s^{-1} and a proportion of false negative events of 18 ± 5%, as revealed by charge recovery analysis (Pernía-Andrade and Jonas, 2014). After detection of individual EPSPs, peak amplitude and kinetics were further evaluated using scripts written in Igor Pro 6.22 (Wavemetrics) and GNU Octave 3.6.× (www.gnu.org/software/octave). Only events with peak amplitudes larger than 5*SD of V_{rest} were considered for further analysis of individual

EPSP properties as their kinetics were satisfactorily fitted. To determine the functional contribution of EPSPs and IPSPs to the recorded compound V_m signal, voltage traces were integrated from previously determined V_{rest} values. Negative deflections were considered IPSPs. Power spectra were calculated using the pwelch function of GNU Octave (data segments of 1-s duration, Hanning windows with a segment overlap of 0.5).

Evaluation of prefiring subthreshold membrane potential oscillations

The power spectra during a time window directly preceding the AP (0–20 ms; t1) and another during a preceding control silent period (100–200 ms; t2) were computed (Fig. 3H). The power spectra were calculated by continuous wavelet transform procedures using a Morlet wavelet (angular frequency = 6).

Passive membrane properties

V_{rest} was determined during baseline CC recordings for epochs with minimal variance of V_m (Pernía-Andrade and Jonas, 2014). In brief, variance and mean of membrane potential were calculated in 100-ms time segments, and plotted against each other for each individual cell (Fig. 3D). The resting membrane potential was then determined from epochs showing minimal variance (10^{th} percentile). Input resistance (R_N) was calculated from the steady-state subthreshold voltage response to 1-s current pulses in a range of ±100 pA (20 pA step size). R_N was defined as the slope of the linear relationship between the amplitude of the voltage response and the injected direct current (DC; Figs. 4A–C). To determine the apparent membrane time constant (τ_m) 1-s DC pulses of −200 pA were applied, and τ_m was estimated from the slow component of a biexponential fit to the associated averaged voltage response following the current offset.

Active membrane properties

To probe the AP phenotype, 1-s depolarizing current pulses were applied (20 or 50 pA increment). When APs were reliably evoked, the first AP of 2–3 consecutive traces was used for analysis. Voltage threshold (thr_V) was defined as the point where the first derivative of V_m first exceeded 20 V s^{-1}. AP peak amplitude and fast after-hyperpolarization (fAHP) amplitude were measured from thr_V. The half-duration of the AP was measured as the duration at half-maximal amplitude. The maximal slope of rise of the AP was determined as the maximum of the first derivative between two consecutive sample points in the AP upstroke. The after-depolarization (ADP) amplitude was measured as the peak V_m relative to V_{rest} in the first 10 ms after the fAHP.

The sag ratio was quantified as the difference between the maximal voltage change during and the mean voltage change at the end of a 1-s current pulse (800–1000 ms), divided by the maximal voltage change (average of ≥ 5 traces, −200 pA current injections).

To determine frequency-current (f–I) relations and to quantitatively analyze spontaneous firing, APs were first automatically located by a threshold-detection algorithm (first derivative of $V_m > 5$ V s^{-1}, 4-sample average, Fig. 2A). Subsequently, nonovershooting spikes in bursts were marked and included. Spikes within bursts were defined using the same method as previously described for spontaneous firing. f–I relations were fit with a logarithmic function including an offset term (Fig. 4K; see Mitchell and Silver, 2003): $f(x) = K\ ln(x) - A$ where f is firing frequency, x is injected current, K is gain, and $\exp[A/k]$ is the offset in x direction.

Data were analyzed with Stimfit 0.10.*x* (Guzman et al., 2014; www.stimfit.org), custom-made scripts in Octave, Igor Pro, and Sigviewer 0.5.*x* (biosig.sourceforge.net). Statistical analysis was performed using nonparametric, two-sided tests (Wilcoxon signed rank test for paired data, Mann-Whitney U test for unpaired data, Bartlett test for homogeneity of variances, Spearman's rank correlation with proper handling of ties, Kruskal-Wallis test for multiple separate populations); a difference was considered significant if the sequential Holm-Bonferroni-corrected significance level was < 0.05 (Zar, 2010; Holm, 1979). All values in text, figures and table are given as mean ± standard error of the mean (SEM), unless stated differently.

RESULTS

To examine the properties of hippocampal principal neurons in their natural network environment, we performed high-resolution whole-cell patch-clamp recordings from neurons in anesthetized rats in vivo (Fig. 1). To confirm the morphological identity and exact location of the neurons, cells were filled with biocytin during recording and subjected to post-hoc labeling (Figs. 1B–D). In total, we recorded from 86 rigorously identified neurons in vivo (55 CA3 pyramidal neurons comprising 14 dendritic and 41 somatic recordings, 13 somatic recordings of CA1 pyramidal neurons, and 18 somatic recordings of dentate gyrus GCs). All cells included in this study were successfully labeled and identified by post-hoc morphological analysis. This analysis considered soma location, as well as general characteristics of the dendritic arborization and axonal projections. The identification of the recording site along the somato-dendritic axis was based on the relative location of the electrode track.

Differential Spontaneous AP Activity in Identified Hippocampal Principal Neurons In Vivo

We first characterized spontaneous firing in the three major types of hippocampal neurons in vivo (Figs. 1E–G). In CA1 and CA3 pyramidal neurons, APs were frequently generated during both light and deep anesthesia (Figs. 1E,F top and middle). In contrast, dentate gyrus GCs were completely silent

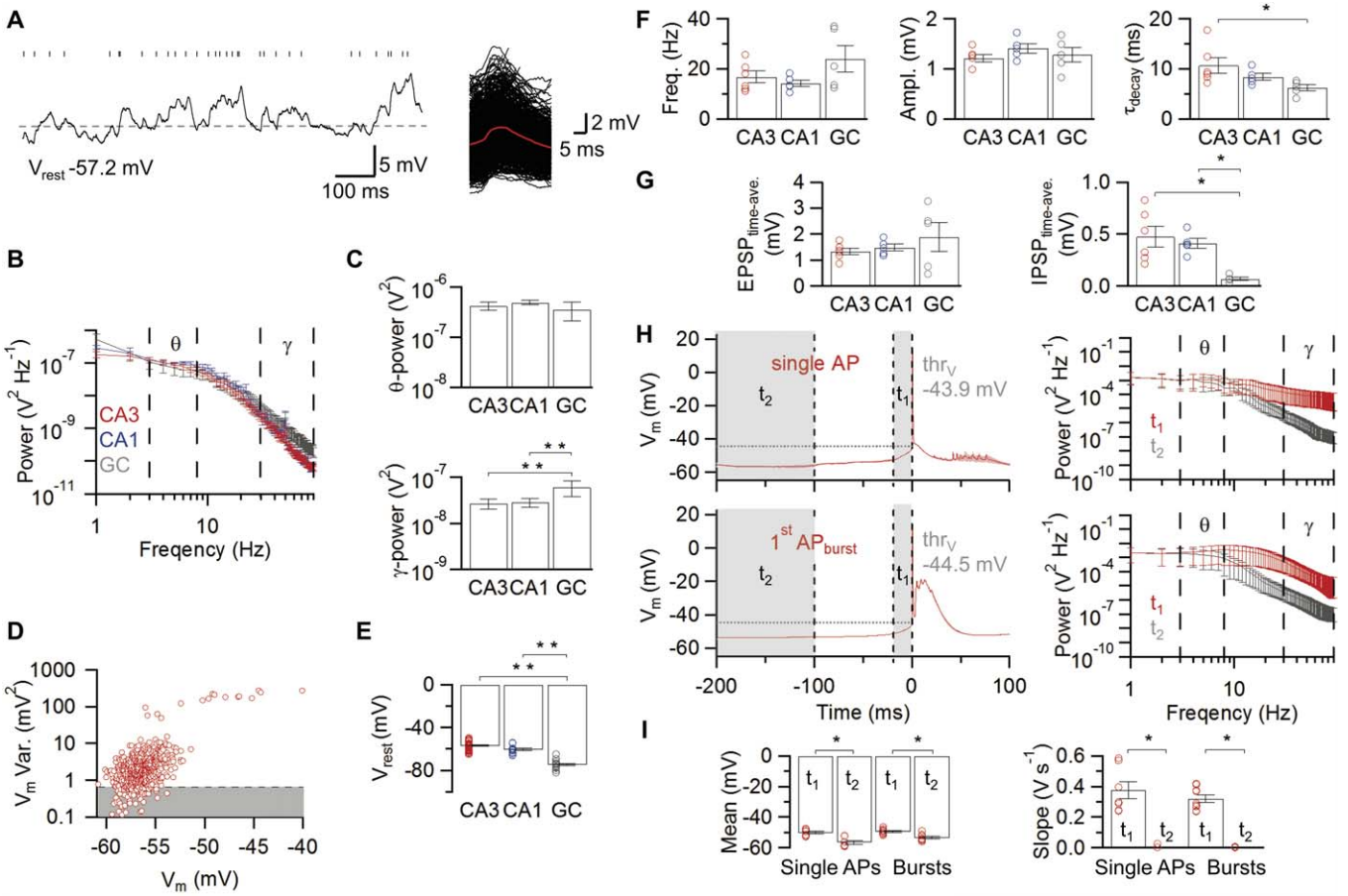

FIGURE 3. Synaptic activity in hippocampal principal neurons in vivo. A: Subthreshold membrane potential fluctuations and EPSP detection in a CA3 pyramidal neuron. Ticks above the trace (left) indicate maxima in the deconvolution trace, which correspond to single EPSPs in the voltage trace. EPSPs detected by the deconvolution-based method are aligned and superimposed according to the detection point (right; averaged EPSP, red). The dashed horizontal line represents the resting membrane potential as estimated with the minimal variance method. B: Average power spectra of subthreshold membrane potential fluctuations in the three types of hippocampal principal neurons. Red, CA3 pyramidal neurons, 9 cells; blue, CA1 pyramidal neurons, 5 cells; gray, GCs, 5 cells. Peaks at 50 Hz are AC artifacts; bars indicate mean values ± SEM. C: Power of subthreshold membrane potential fluctuations in the theta (3–8 Hz; top) and gamma (30–90 Hz; bottom) frequency range. Note that GCs show a higher power of membrane potential fluctuations in the gamma frequency range than CA3 and CA1 pyramidal neurons. D: Variance versus mean analysis of membrane potential fluctuations. Each point represents variance and mean from a 100-ms time window. Shaded area indicates data with variance below the 10th percentile. Outlier points with excess variance correspond to APs. E: Summary bar graph of resting membrane potential determined by the minimal variance method. Note that the resting potential is significantly more depolarized in CA3 and CA1 pyramidal neurons than in GCs. F: Summary bar graph of EPSP frequency (left), peak amplitude (middle), and decay time constant (right). Note that CA3 pyramidal neurons show the slowest EPSP decay time constant, suggesting particularly efficient temporal summation in these cells. G: Summary bar graphs of time-averaged excitatory drive (left) and inhibitory drive (right) obtained by integration of V_m in respect to V_{rest}. Note that the IPSP integral in GCs is minimal, probably due to the shunting nature of inhibition. H,I: Subthreshold membrane potential events preceding AP initiation. H: Spike-triggered group averages for single APs (top left, 20 traces, 7 cells) and bursts (bottom left, 1169 traces, 9 cells) in CA3 pyramidal neurons ± SEM and their respective frequency power spectra (right; t_1, red, t_2, gray) are shown. In (H) as well as in the corresponding summary bar graphs (I) of mean (left) and slope of V_m (right), t_1 indicates a time interval of 20 ms directly preceding single AP or burst; t_2 ranges from 100 to 200 ms before firing and serves as control. Note that, preceding single APs or bursts, the gamma power is increased. Likewise, the membrane potential is significantly depolarized and displays an increased slope, suggesting that preceding EPSPs trigger spiking. Representative traces displaying the gamma modulated V_m depolarization preceding single APs and bursts (t_1) are shown in Figure 1E. Bars indicate mean ± SEM and circles represent values obtained from individual experiments *, $P < 0.05$; **, $P < 0.001$. [Color figure can be viewed in the online issue, which is available at wileyonlinelibrary.com.]

under these conditions (Fig. 1F bottom). To rule out that differences in spontaneous firing of hippocampal principal neurons were caused by the whole-cell recording configuration, we further examined spontaneous firing in the cell-attached configuration (Fig. 1G). Similar to whole-cell recordings, action currents were observed in 6 out of 16 CA3 pyramidal neurons and in 8 out of 12 CA1 pyramidal neurons before break-in, but in none out of 12 dentate gyrus GCs. Thus, differential

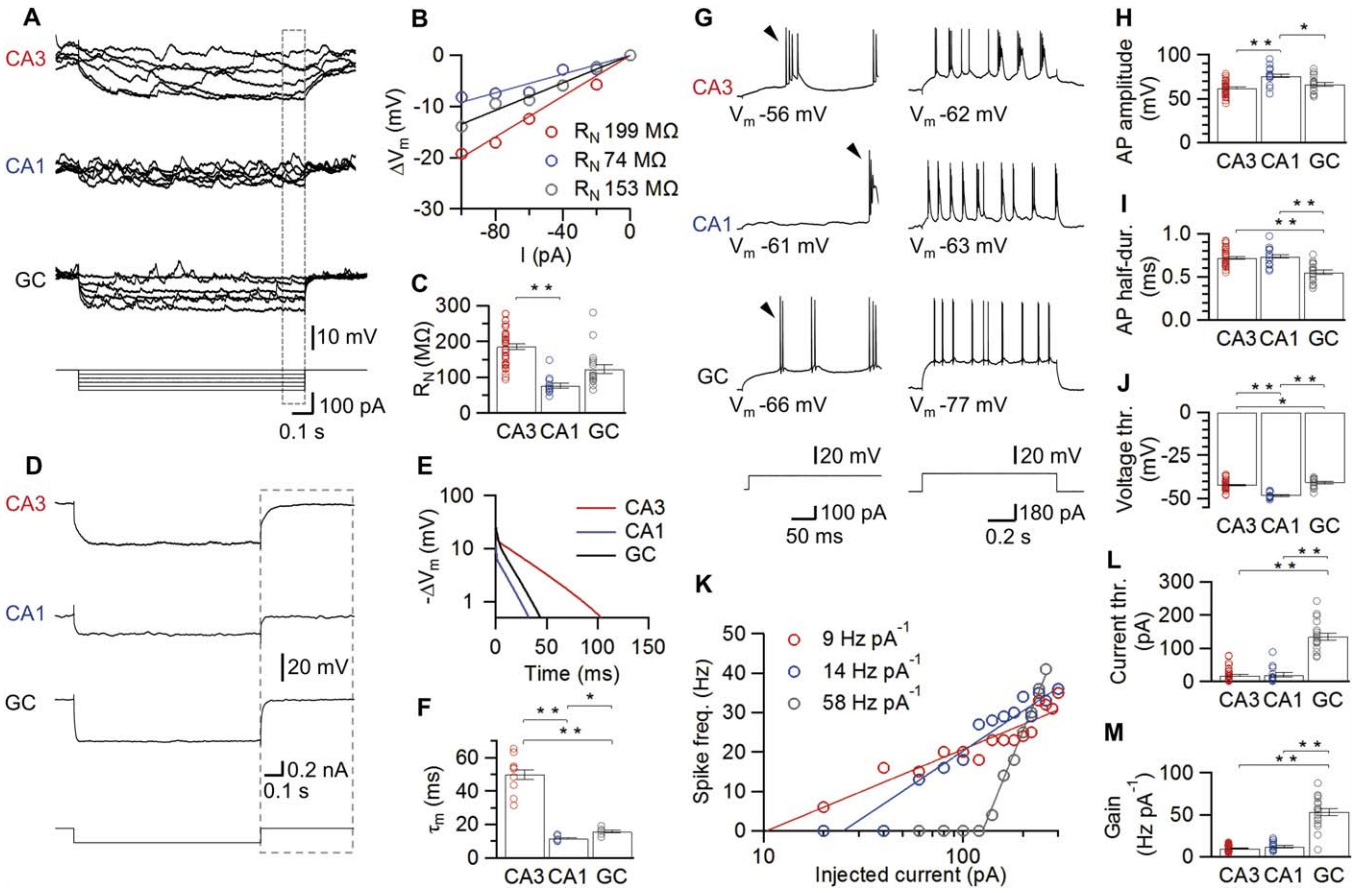

FIGURE 4. Passive and active membrane properties of hippocampal principal neurons in vivo. A–C: Assessment of input resistance (R_N). Typical membrane potential traces (A) in response to 1-s current pulses for a CA3 pyramidal neuron, a CA1 pyramidal neuron, and a dentate gyrus GC and voltage-current relations (B) for the respective neurons. The voltage change was quantified from the last 100 ms of the stimulus (box in A). Summary bar graphs of input resistance for all cell types (C) demonstrate that input resistance is highest in CA3 pyramidal neurons. D–F: Calculation of the membrane time constant (τ_m). Average membrane potential traces for three representative neurons in response to 1-s hyperpolarizing current pulses (−200 pA current injection, A). The boxes in (D) indicate the analysis window after the pulse used for the semi-logarithmic plots of voltage changes in (E). We determined τ_m as the time constant of the slow component from a biexponential fit. Summary bar graphs reveal that CA3 pyramidal neurons had the slowest τ_m. G–M: Cell type-specific active properties of hippocampal principal neurons. G: Firing pattern of hippocampal principal neurons in response to supra-threshold current pulses. (Left, 100 pA; right, 180 pA stimulus amplitude). Arrowheads mark the first AP in the train, which was used for evaluation of evoked AP properties. Note that pyramidal neurons display bursting characteristics resembling those of early bursting CA1/subicular cells (Graves et al., 2012). H–J: Summary bar graphs of evoked AP peak amplitude (H), half-duration (I), and voltage threshold (J). Individual examples of the resulting frequency-current relations for three different, representative neurons (K). Lines represent a semi-logarithmic fit with offset to the data points (Materials and Methods). Bar graphs of current threshold (L), and gain factor (M), with the latter measured as the slope of the fitted function. Note that both voltage and current threshold were lower in CA3 and CA1 pyramidal neurons than in GCs, whereas the gain was highest in GCs. Bars indicate mean ± SEM and circles represent values obtained from individual experiments.*, $P < 0.05$; **, $P < 0.001$. [Color figure can be viewed in the online issue, which is available at wileyonlinelibrary.com.]

spontaneous firing was an intrinsic property of hippocampal principal neurons in vivo.

We next quantified the frequency and time structure of spontaneous AP generation in different hippocampal cell types (Fig. 2). On average, the total spiking frequency was 3.4 ± 0.9 Hz in CA3 pyramidal neurons and 6.4 ± 1.1 Hz in CA1 pyramidal neurons, whereas it was zero in dentate gyrus GCs. Analysis of ISIs in CA3 and CA1 pyramidal neurons against recording time revealed two populations of intervals that differed by almost two orders of magnitude, suggesting that both CA3 and CA1 pyramidal neurons fired in bursts (Fig. 2C). To quantitatively distinguish between single APs and bursts, a critical ISI_{crit} was calculated (Fig. 2D; see Materials and Methods). This analysis revealed a similar critical interval of ~20 ms in both cell types (mean 22.9 ms in CA3 pyramidal neurons; 19.3 ms in CA1 pyramidal neurons). Likewise, the proportion of bursts was similar between these cell types, with 86.5 ± 2.4% in CA3 pyramidal neurons (34 cells) and 96.3 ± 0.8% in CA1 pyramidal neurons (5 cells; Fig. 2I; $P_{CA3\text{-}CA1} > 0.2$; Table 1). Thus, under in vivo conditions,

TABLE 1.

Intrinsic and Synaptic Properties of Hippocampal Principal Neurons In Vivo

	CA3	CA1	GC	$P_{CA3\text{-}CA1}$	$P_{CA1\text{-}GC}$	$P_{CA3\text{-}GC}$
Passive properties, sag ratio						
V_{rest} (mV)	−56.9 ± 0.7 (41)	−60.5 ± 1.1 (13)	−74.7 ± 0.9 (18)	0.010*	<0.001*	<0.001*
Input resistance (MΩ)	186 ± 8 (41)	77 ± 7 (13)	122 ± 13 (18)	<0.001*	0.002*	<0.001*
Membrane time constant (ms)	50 ± 4 (9)	12 ± 1 (6)	16 ± 1 (5)	<0.001*	0.017*	<0.001*
Sag ratio (%)	1.7 ± 0.2 (11)	1.6 ± 0.2 (10)	1.0 ± 0.2 (6)	0.557	0.042	0.015*
Active properties – evoked firing, first AP						
AP voltage threshold (mV)	−42.3 ± 0.4 (41)	−48.4 ± 0.5 (13)	−40.8 ± 0.6 (18)	<0.001*	<0.001*	0.034*
AP current threshold (pA)	18 ± 3 (36)	20 ± 7 (13)	135 ± 11 (18)	0.643	<0.001*	<0.001*
AP amplitude (mV)	62 ± 1 (41)	76 ± 3 (13)	67 ± 2 (18)	<0.001*	0.020*	0.170*
AP half-duration (ms)	0.72 ± 0.02 (41)	0.74 ± 0.03 (13)	0.55 ± 0.02 (18)	0.659	<0.001*	<0.001*
AP max. slope of rise (V s^{-1})	287 ± 11 (41)	500 ± 44 (13)	378 ± 29 (18)	<0.001*	0.047*	0.007*
fast AHP (mV)	3.1 ± 0.4 (6)[a]	–[a]	7.6 ± 0.6 (18)	–	–	0.002*
ADP (mV)	1.2 ± 0.4 (3)[a]	–[a]	5.1 ± 0.7 (7)[a]	–	–	0.033*
Active properties – evoked firing, repetitive spiking properties						
Gain (Hz pA^{-1})	10 ± 1 (36)	12 ± 1 (13)	53 ± 4 (18)	0.272	<0.001*	<0.001*
Spike frequency (Hz)[b]	26.2 ± 1.8 (34)	32 ± 2 (9)	24.5 ± 6 (17)	0.123	0.068	0.223
CV of ISI[b]	1.40 (34)	1.47 (9)	1.15 (13)	0.714	0.110	0.132
Combined AP & burst frequency (Hz)[b]	7.9 ± 0.5 (34)	10.6 ± 0.9 (9)	19.2 ± 5 (17)	0.022*	0.481	0.092
Spikes per burst[b]	4.18 ± 0.34 (34)	3 ± 0.24 (9)	2.64 ± 0.39 (11)[c]	0.182	0.102	0.007*
ISI within burst (ms)[b]	7.8 ± 0.57 (34)	5.1 ± 0.34 (9)	4.06 ± 0.13 (11)[c]	0.016*	0.020*	<0.001*
Spontaneous action potentials and bursts						
Total AP frequency (Hz)	3.4 ± 0.9 (9)	6.4 ± 1.1 (5)	0 (6)	0.083	0.008*	<0.001*
Single AP frequency (Hz)	0.04 ± 0.02 (9)	0.05 ± 0.01 (5)	0 (6)	0.17	0.002*	0.024*
Burst frequency (Hz)	0.7 ± 0.2 (9)	1.4 ± 0.3 (5)	0 (6)	0.147	0.002*	<0.001*
Proportion of bursts (%)	86.5 ± 2.4 (34)	96.3 ± 0.8 (5)	–	0.275	–	–
ISI within burst (ms)	4.9 ± 0.2 (34)	4.7 ± 0.3 (5)	–	0.97	–	–
Spikes per burst	6.4 ± 0.4 (34)	4.2 ± 0.4 (5)	–	0.024*	–	–
Interburst interval (s)	0.76 ± 0.17 (9)	0.27 ± 0.05 (5)	–	0.042*	–	–
Interburst interval distribution τ_1 (ms)	711 ± 10 (9)	237 ± 8 (5)	–	–	–	–
Interburst interval distribution A_1 (%)	75 ± 1 (9)	65 ± 2 (5)	–	–	–	–
Interburst interval distribution τ_2 (s)	3.1 ± 0.1 (9)	1.28 ± 0.05 (5)	–	–	–	–
Interburst interval distribution A_2 (%)	25 ± 1 (9)	34 ± 2 (5)	–	–	–	–
Single AP voltage threshold (mV)	−43.9 ± 0.6 (7)	−47.2 ± 2.3 (3)	–	–	–	–
Single AP peak amplitude (mV)	61 ± 3 (7)	53 ± 1 (3)	–	–	–	–
Single AP half-duration (ms)	0.74 ± 0.05 (7)	0.86 ± 0.02 (3)	–	–	–	–
Single AP max. slope of rise (V s^{-1})	282 ± 27 (7)	235 ± 15 (3)	–	–	–	–
ADP (mV)	0.29 ± 0.12 (7)	0.22 ± 0.12 (3)	–	–	–	–
AP_{burst} voltage threshold (mV)	−44.5 ± 0.6 (9)	−49.7 ± 1.3 (5)	–	0.004*	–	–
AP_{burst} peak amplitude (mV)	61 ± 3 (9)	61 ± 3 (5)	–	>0.9	–	–
AP_{burst} half-duration (ms)	0.75 ± 0.04 (9)	0.82 ± 0.04 (5)	–	0.35	–	–
AP_{burst} max. slope of rise (V s^{-1})	267 ± 28 (9)	322 ± 47 (5)	–	0.438	–	–
Spontaneous EPSPs and IPSPs						
EPSP frequency (Hz)	16.8 ± 2.3 (6)	14.2 ± 1.3 (5)	24.1 ± 5.3 (5)	0.662	0.222	0.247
EPSP peak amplitude (mV)	1.2 ± 0.1 (6)	1.4 ± 0.1 (5)	1.3 ± 0.2 (5)	0.178	0.548	0.662
EPSP 20 − 80% rise time (ms)	3.1 ± 0.1 (6)	3.5 ± 0.1 (5)	2.1 ± 0.1 (5)	0.017*	0.008*	0.004*
EPSP τ_{decay} (ms)	10.7 ± 1.6 (6)	8.4 ± 0.7 (5)	6.2 ± 0.6 (5)	0.247	0.056	0.009*
Time-averaged EPSP amplitude (mV)	1.3 ± 0.1 (6)	1.5 ± 0.1 (5)	1.9 ± 0.5 (5)	0.662	0.691	0.662
Time-averaged IPSP amplitude (mV)	0.48 ± 0.10 (6)	0.41 ± 0.05 (5)	0.07 ± 0.01 (5)	>0.9	0.008*	0.004*

Statistical significance is indicated (*) according to the sequential Holm-Bonferroni correction for three-group comparisons (Materials and Methods). Values in parentheses indicate number of cells. AHP, after-hyperpolarization; ADP, after-depolarization.

[a]Performed if single APs were available.

[b]Evoked by +200 pA current injection.

[c]Calculated if bursts were available.

bursting is more prevalent than single spike activity in both CA3 and CA1 pyramidal neurons.

Additional analysis revealed further differences in the temporal structure of spiking between CA3 and CA1 pyramidal neurons in vivo. First, whereas the ISI within bursts was comparable in the two cell types (4.9 ± 0.2 ms in CA3 versus 4.7 ± 0.3 ms in CA1; Figs. 2E,G; $P > 0.9$), the interburst interval was significantly longer in CA3 pyramidal neurons (0.76 ± 0.17 s in CA3 versus 0.27 ± 0.05 s in CA1; Figs. 2F,H; $P < 0.05$). Second, the number of APs per burst was larger in CA3 than in CA1 pyramidal neurons (6.4 ± 0.4 in CA3 vs. 4.2 ± 0.4 in CA1 pyramidal neurons; Fig. 2J; $P < 0.03$). Thus, bursts in CA3 pyramidal neurons contained a larger number of individual spikes, but were separated by longer time intervals than those in CA1 pyramidal neurons.

Spontaneous Synaptic Activity in Hippocampal Principal Neurons In Vivo

It is often thought that differences in excitatory synaptic drive explain differential spontaneous firing rates in different neuron types (Tsodyks et al., 1999; Epsztein et al., 2011). To test whether differential synaptic activity underlies differential spiking, we next attempted to quantify the frequency of synaptic potentials in the three major hippocampal cell types (Fig. 3). A major challenge in this analysis was the substantial superposition of EPSPs and IPSPs. Power spectrum analysis revealed massive fluctuations of the membrane potential trace in both theta and gamma frequency band (Figs. 3A–C). Whereas the theta power was comparable among different cell types, the gamma power was significantly higher in GCs than in both CA3 and CA1 pyramidal neurons (Fig. 3C), which may be related to a strong gamma coherent inhibitory synaptic input onto GCs (Pernía-Andrade and Jonas, 2014).

To distinguish EPSPs and IPSPs in this fluctuating activity, we first determined V_{rest} by detecting V_m regions with minimal variance (Materials and Methods). On average, V_{rest} was -74.7 ± 0.9 mV in GCs, -60.5 ± 1.1 mV in CA1 pyramidal neurons, and -56.9 ± 0.7 mV in CA3 pyramidal neurons (Fig. 3E; 18, 13, and 41 cells, respectively; $P < 0.001$; Table 1). Thus, the resting potential of GCs is substantially more negative than that of pyramidal neurons in vivo.

We then examined excitatory synaptic activity from V_{rest}. To detect individual EPSPs, we analyzed membrane potential traces by deconvolution, using depolarizing templates (Fig. 3A right). In contrast to our expectations, the frequency of fast EPSPs was not significantly different in the three types of neurons (14.2 ± 1.3 Hz in CA1, 5 cells; 16.8 ± 2.3 Hz in CA3; 6 cells; 24.1 ± 5.3 Hz in GCs, 5 cells; $P > 0.2$; Fig. 3F left; Table 1). Furthermore, the mean EPSP amplitude was comparable among the hippocampal cell types (1.4 ± 0.1 mV in CA1 pyramidal neurons; 1.2 ± 0.1 mV in CA3 pyramidal neurons; 1.3 ± 0.2 mV in GCs; Fig. 3F middle; Table 1). Interestingly, we found significant differences in EPSP decay time constant among the three types of principal neurons, with values of 10.7 ± 1.6 ms in CA3 neurons, 8.4 ± 0.7 ms in CA1 neurons, and 6.2 ± 0.6 ms in GCs (Fig. 3F right; Table 1). Similarly, the 20–80% rise time differed between neurons, with values of 3.1 ± 0.1 ms in CA3 neurons, 3.5 ± 0.1 ms in CA1 neurons, and 2.1 ± 0.1 ms in GCs (Table 1).

Furthermore, we determined the contribution of EPSPs and IPSPs to the fluctuating membrane potential signal. As individual IPSPs are difficult to detect, we used integration of voltage traces from previously determined V_{rest} values. Whereas the integrated strength of excitation was comparable among cell types ($P > 0.6$), the amount of hyperpolarizing inhibition was significantly smaller in GCs than in both CA3 and CA1 pyramidal neurons (Fig. 3G, $P < 0.01$; see Discussion). Taken together, the present results indicate several differences in the excitatory synaptic input among the three hippocampal cell types. However, these differences do not readily explain the differential AP activity in the three cell types (Fig. 2B).

Finally, spike-triggered averages of the membrane potential preceding single APs and bursts in CA3 pyramidal neurons (Figs. 3H,I) revealed a significant increase in depolarizing synaptic input as well as an increase in gamma power in a time window directly preceding the AP (0–20 ms), compared with a control silent period before (100–200 ms). Interestingly, these results are consistent with an elevation of a balanced gamma modulated synaptic input (Atallah and Scanziani, 2009) which may promote the firing of CA3 neurons. However, we observed no differences in the characteristics of the synaptic input between APs and bursts, suggesting that, in both cases, single APs and bursts may be generated by synaptic inputs resulting in similar amplitudes and temporal features when arriving at the soma.

Distinct Passive Membrane Properties of Hippocampal Principal Neurons In Vivo

Next, we examined whether differences in passive membrane properties may contribute to the differential activity of the three types of hippocampal principal neurons in vivo (Fig. 4). Comparative analysis of R_N (see Materials and Methods) of the three cell types revealed it to be highest in CA3 pyramidal neurons, intermediate in dentate gyrus GCs, and lowest in CA1 pyramidal neurons. On average, R_N was 186 ± 8 MΩ in CA3 pyramidal neurons versus 77 ± 7 MΩ in CA1 pyramidal neurons and 122 ± 13 MΩ in GCs (Figs. 4A–C; 41, 13, and 18 cells, respectively; $P \leq 0.002$; Table 1). The difference in R_N among the three cell types appears to be uncorrelated with cell size or surface area, because GCs are much smaller than pyramidal neurons (Schmidt-Hieber et al., 2007). We further examined τ_m in the three neuron types (Figs. 4D–F) to estimate the apparent temporal window for synaptic integration. Voltage responses following a hyperpolarizing current pulse were fit with a sum of two exponential functions, and the time constant of the slow component was taken as a measure of τ_m (see Materials and Methods). Surprisingly, τ_m was markedly slower in CA3 pyramidal neurons than in the two other cell types (Figs. 4E,F). On average, τ_m was 50 ± 2 ms in CA3 pyramidal neurons (9 cells) versus 12 ± 1 ms and 16 ± 1 ms

in CA1 pyramidal neurons and GCs (6 and 5 cells, respectively; $P < 0.001$; Table 1). In conclusion, these results suggest major differences in the specific passive membrane characteristics of the three types of hippocampal principal neurons, with highest input resistance and slowest τ_m in CA3 pyramidal neurons, providing higher excitability and longer synaptic integration windows for these cells.

Different Action Potential Phenotypes of Hippocampal Principal Neurons In Vivo

We examined the active membrane properties and AP phenotypes of the three types of hippocampal principal neurons in vivo (Figs. 4G–M). APs were evoked by 1-s depolarizing current pulses (see Materials and Methods). Representative traces of APs evoked by current pulses and the corresponding summary bar graphs are shown in Figures 4G–J. To characterize the AP phenotype, the average AP frequency was plotted against the injected current, and the corresponding f–I relations were fit with a semi-logarithmic input-output function (Figs. 4K–M, Materials and Methods). The current threshold was quantified as the intersection of the fitted curve with the abscissa, and the gain of the f–I relation was measured as the slope factor of the fitted function.

Comparison of both threshold and gain among the three hippocampal cell types revealed substantial differences in active membrane properties in hippocampal principal neurons. The current threshold was highest in GCs. On average, the threshold value was 20 ± 7 pA in CA1 pyramidal neurons (13 cells) and 18 ± 3 pA in CA3 pyramidal neurons (36 cells) versus 135 ± 11 pA in GCs (18 cells; Fig. 4L; $P < 0.001$; Table 1). Correlatedly, the voltage threshold, defined as the point in the voltage trajectory where the slope exceeded 20 V s^{-1}, was significantly more positive in GCs (-40.8 ± 0.6 mV, see Staley et al., 1992) than in both types of pyramidal neurons (-48.4 ± 0.5 mV in CA1; -42.3 ± 0.4 mV in CA3; Fig. 4J; Table 1). Thus, both current and voltage threshold were higher in GCs than in CA3 or CA1 pyramidal neurons. In contrast, the gain factor was ~5-fold higher in GCs (53 ± 4 Hz pA^{-1}) in comparison to the two pyramidal neuron types (10 ± 1 Hz pA^{-1} in CA3, 12 ± 1 Hz pA^{-1} in CA1; Fig. 4M, Table 1). Thus, whereas CA1 and CA3 pyramidal neurons showed a monotonically rising f–I relationship resembling type I firing, GCs exhibited a marked threshold behavior more reminiscent of type II firing (Ermentrout, 1996).

Surprisingly, all three hippocampal principal cell types showed burst firing during depolarizing current pulses (Fig. 4G). The degree of bursting was quantified by calculating the coefficient of variation (CV) of the ISIs at 200 pA current injection (Table 1). On average, the CV was 1.47, 1.40, and 1.15 in CA1 pyramidal neurons, CA3 pyramidal neurons, and GCs, respectively. Thus, whereas hippocampal principal neurons in vitro are regularly spiking (Spruston and Johnston, 1992), hippocampal principal neurons are intrinsically bursting under in vivo conditions.

Gradients of CA3 Pyramidal Cell Properties In Vivo

Our results revealed major differences between the three major types of hippocampal pyramidal neurons. Are there further differences between subareas? The hippocampal CA3 region is subdivided into subareas referred to as CA3a or distal CA3 (closest to CA1), CA3c or proximal CA3 (in the hilus), and CA3b or middle CA3 (between CA3a and c; Li et al., 1994). To address whether the properties of CA3 pyramidal neurons differ along the transverse CA3a–c axis, we plotted both the passive and active membrane parameters against distance from the border between CA3b and c, based on post-hoc morphological analysis (Figs. 1B–D and 5A–E). Interestingly, with the exception of R_N, the measured active and passive properties showed only minimal changes along the CA3a–c axis [Figs. 5A (top), C–E]. Whereas the resting potential V_{rest} and the voltage threshold of AP initiation were not significantly dependent on distance ($P > 0.5$ in both cases), R_N was significantly correlated with the somatic location along the CA3 axis, with the lowest value in the distal CA3 and the highest value in the proximal CA3 region ($P < 0.01$). Conversely, no significant changes were seen in CA1 cells relative to the CA3b–c boundary (Figs. 5C–E). Likewise, active and passive properties of GCs remained unchanged from the DG crest towards the CA3b–c boundary [$n = 18$; Spearman's rank correlation coefficients (R) for V_{rest}: -0.24 ($P = 0.33$), R_N: 0.07 ($P = 0.80$), and voltage threshold ($Thr._v$): 0.31 ($P = 0.20$)]. Interestingly, the CA3 pyramidal cells showed a positive correlation between 200-pA evoked firing frequency and their somatic location along the stratum oriens–radiatum axis [Figs. 5A (bottom), F–I], suggesting a functional divergence with opposite direction to that reported in CA1 (Mizuseki et al., 2012; Lee et al., 2014). However, neither spontaneous firing nor other CA3 pyramidal cell passive properties showed such correlation, suggesting that the functional divergence in CA3 pyramidal neurons could be generated mainly by their intrinsic active properties instead of the local network activity. Conversely, the CA1 pyramidal cells, which we recorded from (32 ± 6 μm average distance from deep boundary), did not show any significant functional divergence along the oriens–radiatum axis ($n = 13$; R values for V_{rest}, R_N, $Thr._v$, and evoked firing frequency (eFreq) were -0.24 ($P > 0.05$), 0.43 ($P > 0.05$), -0.12 ($P > 0.05$), and 0.24 ($P > 0.05$; $n = 9$), respectively; see Figs. 5F–I). However, the intrinsic properties of CA1 cells are comparable to those reported in slice preparations (Table 1; Spruston and Johnston, 1992; Graves et al., 2012; Lee et al., 2014). Consistent with an enhanced neuronal excitability in younger GCs (Schmidt-Hieber et al., 2004), GCs showed a significant reduction in the evoked firing rate as well as R_N along the hilus–molecular layer axis ($n = 18$; R values for V_{rest}, R_N, $Thr._v$, and eFreq were 0.06 ($P > 0.05$), -0.76 ($P < 0.05$), -0.24 ($P > 0.05$), -0.52 ($P < 0.05$; $n = 17$), respectively, see Figs. 5F–I as reference).

To exclude that the gradients were generated by differences in the subcellular location of the recording electrode, we

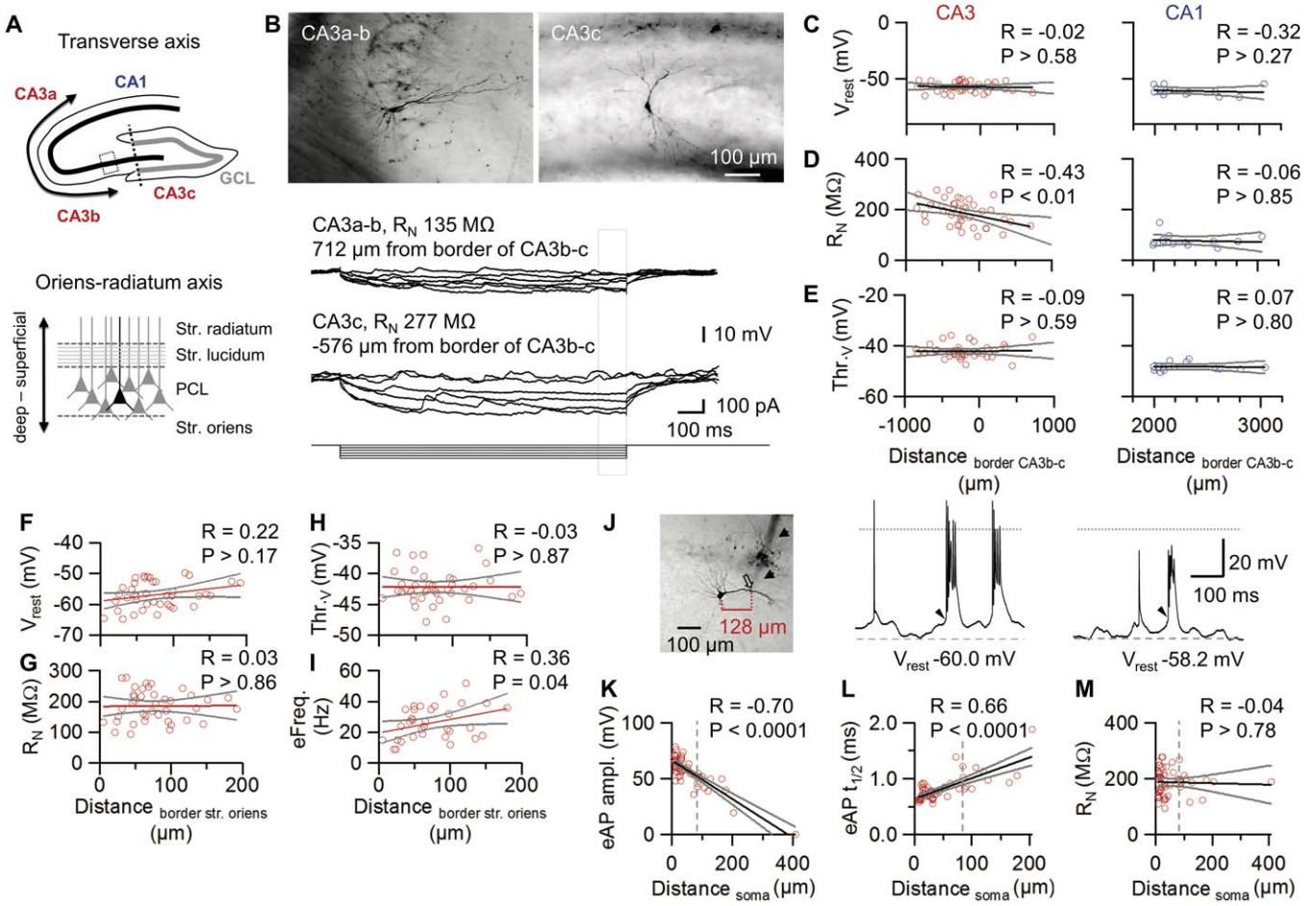

FIGURE 5. Gradient of passive and active properties of CA3 pyramidal neurons along the CA3 a–c axis in vivo. A: Schematic representation of the transverse CA3a–c axis (top; transverse axis, bidirectional arrow) and the CA3 radial axis in the principal cell layer (PCL; bottom; Oriens-ratiatum axis, bidirectional arrow). In top, the CA3b–c boundary is represented as dotted line while the inset box illustrates the CA3 PCL region displayed at the bottom. B: Top, extended focal images of representative CA3 pyramidal neurons recorded at middle-distal CA3 (CA3a–b; left) and proximal CA3 (CA3c; right) pyramidal areas. Bottom, corresponding V_m traces in response to 1-s current pulses (0 to −100 pA). Note the higher input resistance of the CA3c neurons. C–E: Scatter plots of V_{rest} (C), R_N (D), and voltage threshold (E) versus somatic position, measured from the CA3b–c boundary. The CA3 cells ($n = 41$; left) are compared to CA1 cells ($n = 13$; right). Positive values correspond to the middle-distal CA3 region, whereas negative values correspond to the proximal CA3. Note that most of the recordings were performed in the middle and proximal CA3 regions (Li et al., 1994). Distances were measured along the pyramidal cell layer (A top). Gray lines indicate 95% confidence intervals. F–I: Scatter plots of V_{rest} (F), R_N (G), voltage threshold (Thr.,v; H), and evoked firing frequency by 200 pA injected current (eFreq; I) versus somatic position from the deep border of the PCL (A bottom). J: Extended focal image of a CA3 pyramidal neuron in a putative dendritic recording. Note the prominent patch-pipette track (arrows) as well as the dendritic bead caused by patch pipette removal (open arrow, distance from center of soma indicated in red). Whole-cell patch-clamp recordings of spontaneous firing recorded at a soma (middle) and at a dendrite (right). Dashed lines indicate resting potential, dotted lines represent $V_m = 0$. Note that APs are overshooting in the somatic recording, but nonovershooting in the dendritic recording. Additionally, the amplitude of the underlying depolarizing envelope (arrowheads) is enhanced in the dendrite. K–M: Scatter plots of peak amplitude (K), half-duration ($t_{1/2}$, L), and R_N (M) of evoked APs (eAP) vs. distance from center of soma. APs were evoked by depolarizing current injection. Spearman's rank correlation coefficient and P values are indicated on top of each panel. Dashed line indicates separation criterion for < 80 µm (classified as somatic recording) and ≥ 80 µm (classified as dendritic recording), gray lines indicate 95% confidence intervals. [Color figure can be viewed in the online issue, which is available at wileyonlinelibrary.com.]

restricted our analysis to morphologically confirmed somatic recordings. The location of the recording site was determined post-hoc, based on the shape of the electrode track and the presence of a membrane protrusion at the excision site (Materials and Methods). In 14 out of 55 CA3 pyramidal neurons, recordings were made at putative dendritic recording sites, at distances > 80 µm from the center of the soma (Figs. 5J–M). Since these recordings showed smaller AP peak amplitudes and longer half-durations similar to backpropagated APs (Kim et al., 2012), they were not considered for further analysis. In conclusion, our results revealed a functional tangential gradient of CA3 pyramidal neurons along the transverse CA3 axis; the

closer to CA1 the soma was located, the smaller R_N became, approaching the average value for CA1 pyramidal neurons. Furthermore, our analysis demonstrated a small, but significant radial gradient, which is opposite to that previously reported in the CA1 region (Mizuseki et al., 2012; Lee et al., 2014). These results challenge the view that hippocampal CA3 pyramidal neurons represent a functionally uniform cell population.

DISCUSSION

Previous studies in the hippocampal slice preparation revealed that the main types of principal neurons differ in their passive and active membrane properties (Spruston and Johnston, 1992; Major et al., 1994; Lübke et al., 1998; Schmidt-Hieber et al., 2007). Whether these findings can be extrapolated to the in vivo situation where cells are exposed to ongoing synaptic activity and a complex mixture of neuromodulators has remained unknown. Our results demonstrate that certain features are preserved (e.g. input resistance and membrane time constant), whereas others markedly differ between in vivo and in vitro situation (e.g. spontaneous firing and degree of bursting). Furthermore, our results show that hippocampal neuron types in vivo differ from each other in the characteristics of input-output transformation, suggesting cell type-specific information processing in the hippocampal network.

Different Passive and Active Membrane Properties of Hippocampal Principal Neurons In Vivo

Hippocampal principal neurons in vivo markedly differed in their passive membrane properties. Amongst all hippocampal neurons examined, GCs showed the most negative resting potential. In GCs, the average resting potential was close to −80 mV, ∼15 mV more negative than in CA3 or CA1 pyramidal neurons. The specific combination of a relatively low membrane resistance (Figs. 4B,C) and a negative resting membrane potential (Fig. 3E) in GCs is consistent with the idea that a K^+-selective leak conductance generates these specific properties. Although the precise molecular determinants remain to be determined, differential expression of inwardly rectifying K^+ channels (Karschin et al., 1996) or two-pore domain leak K^+ channels may be responsible (Talley et al., 2001).

Amongst all hippocampal neurons examined, CA3 pyramidal neurons showed the highest input resistance and the slowest membrane time constant. An implication of the slow membrane time constant is that CA3 pyramidal neurons will have the widest window for temporal summation. This may facilitate the activation of these neurons by mossy fiber synapses, contributing to the conditional detonator properties of these synapses (Henze et al., 2002; Vyleta and Jonas, 2014). Furthermore, this will facilitate AP initiation by CA3–CA3 cell synapses, which only have small unitary EPSP peak amplitudes (Miles and Wong, 1986). These passive properties may be relevant for pattern completion, one of the putative functions of CA3 pyramidal neurons in the hippocampal network (Marr, 1971; Nakazawa et al., 2002).

Hippocampal principal neurons in vivo also differed substantially in their active membrane properties. Intriguingly, GCs show the highest current and voltage threshold for AP initiation. At the same time, GCs exhibit the highest gain of the input-output curve. Thus, GCs will be mostly silent in the absence of synaptic input, but are able to fire at high frequencies following strong synaptic stimulation. Whereas CA1 and CA3 pyramidal neurons show a monotonically rising f–I relationship resembling type I firing, GCs exhibited a marked threshold behavior reminiscent of type II firing (Ermentrout, 1996). The type II firing of GCs may be useful for pattern separation, one of the putative functions of GCs in the hippocampal network (Leutgeb et al., 2007; de Almeida et al., 2009a).

Different Spontaneous Action Potential Activity in Hippocampal Neurons In Vivo

A major difference between hippocampal principal neurons in vivo and in slices is the presence of spontaneous firing under in vivo conditions. Whereas GCs are silent in anesthetized animals, both CA3 and CA1 pyramidal neurons in the intact network generate APs with a frequency of ∼5 Hz (Fig. 2B). Interestingly, the overall spontaneous firing frequency recorded in CA3 and CA1 pyramidal neurons is comparable to that recorded with extracellular electrodes in rats during slow wave sleep, REM sleep, and running (Mizuseki and Buzsáki, 2009), consistent with the evidence of a preserved firing rate of principal neurons across different brain states.

What are the triggers of AP activity in CA3 and CA1 pyramidal neurons? Our analysis reveals that hippocampal pyramidal neurons are exposed to a fluctuating barrage of EPSPs and IPSPs. These membrane potential fluctuations show both theta and gamma frequency components, and may collectively underlie theta–gamma oscillations in the field potential (Pernía-Andrade and Jonas, 2014). Analysis of baseline membrane potential activity preceding APs reveals that the membrane potential before the spikes is more depolarized, has a larger variance, and shows a depolarizing trajectory. All these data are consistent with the hypothesis that incoming EPSPs trigger AP activity in CA3 and CA1 pyramidal neurons.

What are the mechanisms underlying the differential activity, that is the high activity in CA3 and CA1 pyramidal neurons versus the sparse AP generation in GCs? Several mechanisms are conceivable: (1) a higher level of synaptic excitation in pyramidal neurons, (2) a lower level of synaptic inhibition, (3) different passive integration properties of the cells, and (4) differential excitability. Surprisingly, the amplitude and frequency of these EPSP fluctuations is not significantly different between the three types of hippocampal principal neurons and IPSP amplitude is actually lowest in GCs (Fig. 3G). Furthermore, the smaller amount of hyperpolarizing inhibition recorded in

GCs than in CA3 and CA1 cells supports the evidence of a differential inhibitory control in the three hippocampal subregions, where inhibition is predominantly hyperpolarizing in CA1 and CA3 principal cells whereas it is more depolarizing or shunting in GCs (Chiang et al., 2012; Sauer et al., 2012). Thus, the differential activity of cells does not seem related to frequency or amplitude of synaptic input. Furthermore, the passive properties are unlikely to be the sole mechanism determining the firing phenotype, because input resistance and membrane time constant differ substantially between CA3 and CA1 cells (which are both spontaneously active in vivo). However, the combination of lower membrane potential and the higher AP threshold in GCs may lead to a situation where the probability that fluctuating EPSP–IPSP sequences cross the AP threshold is extremely low. Thus, our results emphasize the importance of cell type-specific excitability for shaping activity patterns in vivo.

Prevalence of Burst Firing in Hippocampal Neurons In Vivo

A major difference between hippocampal principal neurons in vivo and in slices is the high proportion of bursts under in vivo conditions. This confirms and extends previous findings for hippocampal GCs (Pernía-Andrade and Jonas, 2014) and CA1 pyramidal neurons (Epsztein et al., 2011; Grienberger et al., 2014) using whole-cell patch-clamp recordings in anesthetized and awake animals. However, the proportion of bursts recorded in CA1 and CA3 pyramidal cells in our experiments is markedly higher than that estimated by extracellular recordings from awake, freely moving animals (Harris et al., 2000, 2001; Buzsáki, 2004; Mizuseki and Buzsáki, 2009). Several reasons may account for this apparent discrepancy. First, late spikes within bursts will be reliably detected with whole-cell recording, but may be missed in extracellular recordings. Second, general anesthetics may change the abundance of bursting. However, we did not detect any major differences in the proportion of bursting between two different forms of anesthesia acting on different molecular targets and between anesthetized and awake animals (GCs: Pernía-Andrade and Jonas, 2014; CA3 pyramidal neurons: J.K., unpublished). Anesthetics promote burst firing in thalamic neurons, which could be relayed to higher cortical areas (Franks, 2008). However, the thalamic nucleus reuniens, the major thalamic input to the hippocampus, provides glutamatergic projections to CA1, but avoids both CA3 and dentate gyrus (Wouterlood et al., 1990; Vertes et al., 2007). More work on awake, freely moving animals will be needed to address the abundance of bursting in different behavioral conditions.

What are the mechanisms underlying bursting? Both intrinsic (Azouz et al., 1996; Metz et al., 2005; Moore et al., 2009) and synaptic mechanisms (NMDA spikes; Grienberger et al., 2014) have been suggested (see Traub and Miles, 1991). Interestingly, the intrinsic excitability of pyramidal neurons is regulated by metabotropic glutamate and muscarinic acetylcholine receptors, such that while the activation of mGluR1 receptors and muscarinic ACh receptors promotes burst firing, the activation of mGluR5 inhibits burst firing in subicular neurons in vitro in the slice preparation (Moore et al., 2009). Other evidence from slice preparations suggests that the usage of an extracellular physiological solution with 1.2 mM Ca^{2+} and 3.5 mM K^{+} at physiological temperature is sufficient to facilitate spontaneous bursting in CA3 pyramidal cells (Kowalski et al., 2012). Thus, it is tempting to speculate that under in vivo conditions, the abundant presence of neuromodulators as well as slightly different extracellular Ca^{2+} and K^{+} concentrations switch CA3 and CA1 neurons into a burst firing mode entirely, such that bursting becomes the default activity in the intact network.

Implications for Network Function and Coding

Pattern separation (Leutgeb et al., 2007; de Almeida et al., 2009a) and pattern completion (Marr, 1971; Nakazawa et al., 2002) are believed to be major functions of the hippocampal network. How are these network functions shaped by the specific single-cell properties of hippocampal principal neurons?

The characteristic passive and active membrane properties of GCs in vivo may be critically important for pattern separation in the dentate gyrus (Leutgeb et al., 2007). For example, the negative resting potential and the high activation threshold of GCs directly translate into sparse coding, a hallmark property of activity in the dentate gyrus in vivo. Furthermore, these cellular properties may contribute to the "winner takes all" function of the dentate gyrus, complementing the role of recurrent inhibition (de Almeida et al., 2009a).

Similarly, the passive and active properties of CA3 pyramidal neurons may be relevant for pattern completion. The uniquely slow membrane time constant and the high input resistance of CA3 cells will increase the efficacy of excitatory input synapses and prolong the windows for temporal EPSP summation. These properties may be useful for the retrieval of incomplete patterns in the auto-associative CA3 cell network, especially under conditions when individual cells in an ensemble fire slightly asynchronously. Furthermore, these properties may help the relatively weak CA3–CA3 cell synapses (Miles and Wong, 1986) to efficiently retrieve patterns, as proposed in several models of pattern completion (Marr, 1971; Treves and Rolls, 1994).

Finally, the high proportion of bursts in CA3 and CA1 pyramidal neurons has major implications for coding and plasticity induction in the hippocampus (Lisman, 1997; Pike et al., 1999; Izhikevich et al., 2003; Xu et al., 2012). Interestingly, the proportion of bursts in vivo (Fig. 2) is higher in the hippocampus than in other areas of the brain, such as entorhinal cortex (Mizuseki et al., 2011) and prefrontal cortex (Fujisawa et al., 2008). Thus, burst coding seems highly abundant in the hippocampus, but less prevalent in other areas of the brain. Burst coding will enhance synaptic output, increasing the efficacy of weak synapses. Interestingly, knockdown of synaptotagmin 1 (the Ca^{2+} sensor of exocytosis), which alters the output to single APs, but leaves the output to bursts unchanged,

affects behavioral learning in a region-specific way. Synaptotagmin 1 knockdown reduces the performance of a prefrontal cortex-dependent remote memory recall, but does not perturb hippocampus-dependent contextual fear conditioning (Xu et al., 2012). Our results provide a direct explanation for this previous finding: The abundance of burst coding in CA3 and CA1 pyramidal neurons in vivo.

Acknowledgments

The authors thank José Guzmán for critically reading prior versions of the manuscript. They also thank T. Asenov for engineering mechanical devices, A. Schlögl for efficient programming, F. Marr for technical assistance, and E. Kramberger for manuscript editing.

REFERENCES

Amaral D. 1978. A Golgi study of cell types in the hilar region of the hippocampus in the rat. J Comp Neurol 182:851–914.

Andersen P, Bliss TVP, Skrede KK. 1971. Lamellar organization of hippocampal pathways. Exp Brain Res 13:222–238.

Atallah B, Scanziani M. 2009. Instantaneous modulation of gamma oscillation frequency by balancing excitation with inhibition. Neuron 62:566–577.

Azouz R, Jensen MS, Yaari Y. 1996. Ionic basis of spike afterdepolarization and burst generation in adult rat hippocampal CA1 pyramidal cells. J Physiol 492:211–223.

Buzsáki G. 2004. Large-scale recording of neuronal ensembles. Nat Neurosci 7:446–451.

Chiang P-H, Wu P-Y, Kuo T-W, Liu Y-C, Chan C-F, Chien T-C, Cheng J-K, Huang Y-Y, Chiu C-D, Lien C-C. 2012. GABA is depolarizing in hippocampal dentate granule cells of the adolescent and adult rats. J Neurosci 32:62–67.

de Almeida L, Idiart M, Lisman JE. 2009a. A second function of gamma frequency oscillations: An E%-max winner-take-all mechanism selects which cells fire. J Neurosci 29:7497–7503.

de Almeida L, Idiart M, Lisman JE. 2009b. The input-output transformation of the hippocampal granule cells: From grid cells to place fields. J Neurosci 29:7504–7512.

Epsztein J, Brecht M, Lee AK. 2011. Intracellular determinants of hippocampal CA1 place and silent cell activity in a novel environment. Neuron 70:109–120.

Ermentrout B. 1996. Type I membranes, phase resetting curves, and synchrony. Neural Comput 8:979–1001.

Fujisawa S, Amarasingham A, Harrison MT, Buzsáki G. 2008. Behavior-dependent short-term assembly dynamics in the medial prefrontal cortex. Nat Neurosci 11:823–833.

Franks N. 2008. General anaesthesia: from molecular targets to neuronal pathways of sleep and arousal. Nat Rev Neurosci 9:370–386.

Graves A, Moore S, Bloss E, Mensh B, Kath W, Spruston N. 2012. Hippocampal pyramidal neurons comprise two distinct cell types that are countermodulated by metabotropic receptors. Neuron 76: 776–789.

Grienberger C, Chen X, Konnerth A. 2014. NMDA receptor-dependent multidendrite Ca^{2+} spikes required for hippocampal burst firing *in vivo*. Neuron 81:1274–1281.

Guzman SJ, Schlögl A, Schmidt-Hieber C. 2014. Stimfit: Quantifying electrophysiological data with Python. Front Neuroinform 8:16.

Hafting T, Fyhn M, Molden S, Moser M-B, Moser EI. 2005. Microstructure of a spatial map in the entorhinal cortex. Nature 436: 801–806.

Harris KD, Henze DA, Csicsvari J, Hirase H, Buzsáki G. 2000. Accuracy of tetrode spike separation as determined by simultaneous intracellular and extracellular measurements. J Neurophysiol 84: 401–414.

Harris KD, Hirase H, Leinekugel X, Henze DA, Buzsáki G. 2001. Temporal interaction between single spikes and complex spike bursts in hippocampal pyramidal cells. Neuron 32:141–149.

Henze DA, Wittner L, Buzsáki G. 2002. Single granule cells reliably discharge targets in the hippocampal CA3 network *in vivo*. Nat Neurosci 5:790–795.

Holm S. 1979. A simple sequentially rejective multiple test procedure. Scand J Stat 6:65–70.

Izhikevich EM, Desai NS, Walcott EC, Hoppensteadt FC. 2003. Bursts as a unit of neural information: selective communication via resonance. Trends Neurosci 26:161–167.

Karschin C, Dissmann E, Stühmer W, Karschin A. 1996. IRK(1-3) and GIRK(1-4) inwardly rectifying K^+ channel mRNAs are differentially expressed in the adult rat brain. J Neurosci 16:3559–3570.

Kim S, Guzman SJ, Hu H, Jonas P. 2012. Active dendrites support efficient initiation of dendritic spikes in hippocampal CA3 pyramidal neurons. Nat Neurosci 15:600–606.

Kowalski J, Kim S, Gan J, Pernía-Andrade A, Frotscher M, Jonas P. 2012. Bursting of CA3 pyramidal neurons in rat hippocampus *in vivo*. Neuroscience Meeting Planner, Program No. 648.03. Society for Neuroscience, Washington, DC. [Online].

Lee A, Manns I, Sakmann B, Brecht M. 2006. Whole-cell recordings in freely moving rats. Neuron 51:399–407.

Lee S, Marchionni I, Bezaire M, Varga C, Danielson N, Lovett-Barron M, Losonczy A, Soltesz I. 2014. Parvalbumin-positive basket cells differentiate among hippocampal pyramidal cells. Neuron 82:1129–1144.

Leutgeb JK, Leutgeb S, Moser M-B, Moser EI. 2007. Pattern separation in the dentate gyrus and CA3 of the hippocampus. Science 315:961–966.

Li XG, Somogyi P, Ylinen A, Buzsáki G. 1994. The hippocampal CA3 network: An *in vivo* intracellular labeling study. J Comp Neurol 339:181–208.

Lisman JE. 1997. Bursts as a unit of neural information: Making unreliable synapses reliable. Trends Neurosci 20:38–43.

Lisman JE. 1999. Relating hippocampal circuitry to function: Recall of memory sequences by reciprocal dentate-CA3 interactions. Neuron 22:233–242.

Lübke J, Frotscher M, Spruston N. 1998. Specialized electrophysiological properties of anatomically identified neurons in the hilar region of the rat fascia dentata. J Neurophysiol 79:1518–1534.

Major G, Larkman AU, Jonas P, Sakmann B, Jack JJB. 1994. Detailed passive cable models of whole-cell recorded CA3 pyramidal neurons in rat hippocampal slices. J Neurosci 14:4613–4638.

Margrie TW, Brecht M, Sakmann B. 2002. *In vivo*, low-resistance, whole-cell recordings from neurons in the anaesthetized and awake mammalian brain. Pflüg Arch Eur J Physiol 444:491–498.

Marr D. 1971. Simple memory: A theory for archicortex. Philos Trans R Soc Lond B Biol Sci 262:23–81.

Metz AE, Jarsky T, Martina M, Spruston N. 2005. R-type calcium channels contribute to afterdepolarization and bursting in hippocampal CA1 pyramidal neurons. J Neurosci 25:5763–5773.

Miles R, Wong RKS. 1986. Excitatory synaptic interactions between CA3 neurones in the guinea-pig hippocampus. J Physiol 373:397–418.

Mitchell SJ, Silver RA. 2003. Shunting inhibition modulates neuronal gain during synaptic excitation. Neuron 38:433–445.

Mizuseki K, Sirota A, Pastalkova E, Buzsaki G. 2009. Theta oscillations provide temporal windows for local circuit computation in the entorhinal-hippocampal loop. Neuron 64:267–280.

Mizuseki K, Diba K, Pastalkova E, Buzsaki G. 2011. Hippocampal CA1 pyramidal cells form functionally distinct sublayers. Nat Neurosci 14:1174–1181.

Mizuseki K, Royer S, Diba K, Buzsaki G. 2012. Activity dynamics and behavioral correlates of CA3 and CA1 hippocampal pyramidal neurons. Hippocampus 22:1659–1680.

Mizuseki K, Buzsaki G. 2013. Preconfigured, skewed distribution of firing rates in the hippocampus and entorhinal cortex. Cell Rep 4: 1010–1021.

Moore SJ, Cooper DC, Spruston N. 2009. Plasticity of burst firing induced by synergistic activation of metabotropic glutamate and acetylcholine receptors. Neuron 61:287–300.

Nakazawa K, Quirk MC, Chitwood RA, Watanabe M, Yeckel MF, Sun LD, Kato A, Carr CA, Johnston D, Wilson MA, Tonegawa S. 2002. Requirement for hippocampal CA3 NMDA receptors in associative memory recall. Science 297:211–218.

O'Keefe J, Dostrovsky J. 1971. The hippocampus as a spatial map. Preliminary evidence from unit activity in the freely-moving rat. Brain Res 34:171–175.

Pernía-Andrade AJ, Jonas P. 2014. Theta-Gamma-modulated synaptic currents in hippocampal granule cells *in vivo* define a mechanism for network oscillations. Neuron 81:140–152.

Pernía-Andrade AJ, Goswami SP, Stickler Y, Fröbe U, Schlögl A, Jonas P. 2012. A Deconvolution-based method with high sensitivity and temporal resolution for detection of spontaneous synaptic currents *in vitro* and *in vivo*. Biophys J 103:1429–1439.

Pike FG, Meredith RM, Olding AW, Paulsen O. 1999. Postsynaptic bursting is essential for 'Hebbian' induction of associative long-term potentiation at excitatory synapses in rat hippocampus. J Physiol 518:571–576.

Rolls ET. 2013. The mechanisms for pattern completion and pattern separation in the hippocampus. Front Syst Neurosci 7:74.

Sauer JF, Strüber M, Bartos M. 2012. Interneurons provide circuit-specific depolarization and hyperpolarization. J Neurosci 32:4224–4229.

Scharfman HE. 1993. Spiny neurons of area CA3c in rat hippocampal slices have similar electrophysiological characteristics and synaptic responses despite morphological variation. Hippocampus 3:9–28.

Schmidt-Hieber C, Jonas P, Bischofberger J. 2004. Enhanced synaptic plasticity in newly generated granule cells of the adult hippocampus. Nature 429:184–187.

Schmidt-Hieber C, Jonas P, Bischofberger J. 2007. Subthreshold dendritic signal processing and coincidence detection in dentate gyrus granule cells. J Neurosci 27:8430–8441.

Scoville WB, Milner B. 1957. Loss of recent memory after bilateral hippocampal lesions. J Neurol Neurosurg Psychiatry 20:11–21.

Spruston N, Johnston D. 1992. Perforated patch-clamp analysis of the passive membrane properties of three classes of hippocampal neurons. J Neurophysiol 67:508–529.

Staley KJ, Otis TS, Mody I. 1992. Membrane properties of dentate gyrus granule cells: Comparison of sharp microelectrode and whole-cell recordings. J Neurophysiol 67:1346–1358.

Talley EM, Solorzano G, Lei Q, Kim D, Bayliss DA. 2001. CNS distribution of members of the two-pore-domain (KCNK) potassium channel family. J Neurosci 21:7491–7505.

Traub R, Miles R. 1991. Neuronal networks of the hippocampus. New York: Cambridge University Press New York.

Treves A, Rolls ET. 1994. Computational analysis of the role of the hippocampus in memory. Hippocampus 4:374–391.

Tsodyks M, Kenet T, Grinvald A, Arieli A. 1999. Linking spontaneous activity of single cortical neurons and the underlying functional architecture. Science 286:1943–1946.

Vertes R, Hoover W, Szigeti-Buck K, Leranth C. 2007. Nucleus reuniens of the midline thalamus: Link between the medial prefrontal cortex and the hippocampus. Brain Res Bull 71:601–609.

Vyleta NP, Jonas P. 2014. Loose coupling between Ca^{2+} channels and release sensors at a plastic hippocampal synapse. Science 343:665–670.

Xu W, Morishita W, Buckmaster PS, Pang ZP, Malenka RC, Südhof TC. 2012. Distinct neuronal coding schemes in memory revealed by selective erasure of fast synchronous synaptic transmission. Neuron 73:990–1001.

Wouterlood F, Saldana E, Witter M. 1990. Projection from the nucleus reuniens thalami to the hippocampal region: light and electron microscopic tracing study in the rat with the anterograde tracer Phaseolus vulgaris-leucoagglutinin. J Comp Neurol 296:179–203.

Zar JH. 2010. Biostatistical analysis. Upper Saddle River: NJ. Prentice-Hall/Pearson.